

Simultaneous X-ray and radio observations of the transitional millisecond pulsar candidate CXOU J110926.4–650224

The discovery of a variable radio counterpart

F. Coti Zelati^{1,2,3}, B. Hugo^{4,5}, D. F. Torres^{1,2,6}, D. de Martino⁷, A. Papitto⁸, D. A. H. Buckley^{9,10,11}, T. D. Russell¹², S. Campana³, R. Van Rooyen⁴, E. Bozzo¹³, C. Ferrigno¹³, J. Li^{14,15}, S. Migliari^{16,17}, I. Monageng^{11,9}, N. Rea^{1,2}, M. Serylak^{4,18}, B. W. Stappers¹⁹, and N. Titus^{11,9}

¹ Institute of Space Sciences (ICE, CSIC), Campus UAB, Carrer de Can Magrans s/n, 08193 Barcelona, Spain
e-mail: cotizelati@ice.csic.es

² Institut d'Estudis Espacials de Catalunya (IEEC), Carrer Gran Capità 2–4, 08034 Barcelona, Spain

³ INAF–Osservatorio Astronomico di Brera, Via Bianchi 46, 23807 Merate, LC, Italy

⁴ South African Radio Astronomy Observatory, 2 Fir Street, Black River Park, Observatory, Cape Town 7925, South Africa

⁵ Department of Physics and Electronics, Rhodes University, PO Box 94, Grahamstown 6140, South Africa

⁶ Institució Catalana de Recerca i Estudis Avançats (ICREA), Passeig Luíís Companys 23, 08010 Barcelona, Spain

⁷ INAF – Osservatorio Astronomico di Capodimonte, Salita Moiariello 16, 80131 Napoli, Italy

⁸ INAF – Osservatorio Astronomico di Roma, Via Frascati 33, 00040 Monte Porzio Catone, Roma, Italy

⁹ South African Astronomical Observatory, PO Box 9, 7935 Observatory, Cape Town, South Africa

¹⁰ Department of Physics, University of the Free State, PO Box 339, Bloemfontein, 9300, South Africa

¹¹ Department of Astronomy, University of Cape Town, Private Bag X3, Rondebosch 7701, South Africa

¹² INAF–Istituto di Astrofisica Spaziale e Fisica Cosmica, Via U. La Malfa 153, 90146 Palermo, Italy

¹³ Department of Astronomy, University of Geneva, Chemin d'Ecogia 16, 1290 Versoix, Switzerland

¹⁴ CAS Key Laboratory for Research in Galaxies and Cosmology, Department of Astronomy, University of Science and Technology of China, No. 96 JinZhai Road Baohe District, Hefei 230026, Anhui, PR China

¹⁵ School of Astronomy and Space Science, University of Science and Technology of China, No. 96 JinZhai Road Baohe District, Hefei 230026, Anhui, PR China

¹⁶ Aurora Technology BV for the European Space Agency, ESAC/ESA, Camino Bajo del Castillo s/n, Urb. Villafranca del Castillo, 28691 Villanueva de la Cañada, Madrid, Spain

¹⁷ Institute of Cosmos Sciences, University of Barcelona, Martí i Franquès 1, 08028 Barcelona, Spain

¹⁸ Department of Physics and Astronomy, University of the Western Cape, Bellville, Cape Town 7535, South Africa

¹⁹ Jodrell Bank Centre for Astrophysics, Department of Physics and Astronomy, The University of Manchester, Alan Turing Building, Oxford Road, Manchester M13 9PL, UK

Received 31 May 2021 / Accepted 23 September 2021

ABSTRACT

We present the results of simultaneous observations of the transitional millisecond pulsar (tMSP) candidate CXOU J110926.4–650224 with the *XMM-Newton* satellite and the MeerKAT telescope. The source was found at an average X-ray luminosity of $L_X \approx 7 \times 10^{33}$ erg s⁻¹ over the 0.3–10 keV band (assuming a distance of 4 kpc) and displayed a peculiar variability pattern in the X-ray emission, switching between high, low and flaring modes on timescales of tens of seconds. A radio counterpart was detected at a significance of 7.9σ with an average flux density of ≈ 33 μ Jy at 1.28 GHz. It showed variability over the course of hours and emitted a ≈ 10 -min long flare just a few minutes after a brief sequence of multiple X-ray flares. No clear evidence for a significant correlated or anticorrelated variability pattern was found between the X-ray and radio emissions over timescales of tens of minutes and longer. CXOU J110926.4–650224 was undetected at higher radio frequencies in subsequent observations performed with the Australia Telescope Compact Array, when the source was still in the same X-ray sub-luminous state observed before, down to a flux density upper limit of 15 μ Jy at 7.25 GHz (at 3σ). We compare the radio emission properties of CXOU J110926.4–650224 with those observed in known and candidate tMSPs and discuss physical scenarios that may account for its persistent and flaring radio emissions.

Key words. accretion, accretion disks – ISM: jets and outflows – pulsars: general – radio continuum: stars – stars: neutron – X-rays: binaries

1. Introduction

Transitional millisecond pulsars (tMSPs) are weakly magnetized ($B \approx 10^8$ – 10^9 G) neutron stars (NSs) in binary systems that spin hundreds of times per second and swing between different emission regimes, depending on the mass transfer rate from their

low-mass ($< 1 M_\odot$) non-degenerate companion star. When the mass transfer is low or even switches off, the tMSPs are detected as MSP binaries with low X-ray luminosities ($L_X \lesssim 10^{32}$ erg s⁻¹) and with no evidence for the presence of an accretion disk (e.g. Archibald et al. 2009; de Martino et al. 2020 and references therein). Their emission from the radio to the gamma-ray band

is powered mostly by the pulsar rotational energy and an intra-binary shock that forms due to the interaction between the wind of relativistic particles ejected by the pulsar and matter transferred from the companion (for a review, see [Harding 2021](#)). At higher mass transfer rates, the tMSPs are observed in a X-ray sub-luminous state ($L_X \approx 10^{33} - 10^{34} \text{ erg s}^{-1}$) characterised by the presence of an accretion disk around the NS and by peculiar multiband properties (see below), probably connected with the presence of an active rotation-powered MSP inhibiting accretion onto the NS (e.g. [Ambrosino et al. 2017](#); [Bogdanov et al. 2018](#); [Papitto et al. 2019](#); [Veledina et al. 2019](#); [Campana et al. 2019](#); [Jaodand et al. 2021](#)). In one case, a month-long bright X-ray outburst ($L_X \gtrsim 10^{36} \text{ erg s}^{-1}$) powered by mass accretion onto the NS surface was also observed ([Papitto et al. 2013](#)). The tMSPs can linger in the rotation-powered state or the X-ray sub-luminous state for decades, and perform a transition on timescales of weeks (or even shorter), following a change in the mass transfer rate from the companion ([Stappers et al. 2014](#); [Bassa et al. 2014](#)). Three tMSPs are known to date (for reviews, see [Campana & Di Salvo 2018](#); [Papitto & de Martino 2020](#)).

The tMSPs display enigmatic phenomenological properties in the X-ray sub-luminous state. These include: a unique variability pattern in the X-ray emission, which manifests in the form of repeated switches between three intensity levels (henceforth dubbed ‘high’, ‘low’ and ‘flaring’ modes) on timescales of tens of seconds; gamma-ray emission detectable with the *Fermi* satellite up to GeV energies at a luminosity of $L_\gamma \approx 10^{33} - 10^{34} \text{ erg s}^{-1}$, comparable to that in the X-ray band; flaring activity and flickering at optical and near infrared wavelengths reminiscent of the X-ray mode transitions; relatively bright, variable radio continuum emission with a flat to slightly inverted spectrum ([Hill et al. 2011](#); [Ferrigno et al. 2014](#); [Deller et al. 2015](#)). This latter emission has been interpreted in terms of partially self-absorbed synchrotron radiation from a population of relativistic electrons that are launched in the form of a weak steady, compact jet (e.g. [Blandford & Königl 1979](#); [Blandford & Payne 1982](#)), possibly in the presence of a quickly rotating NS magnetosphere that propels away the in-flowing plasma ([Papitto & Torres 2015](#); [Deller et al. 2015](#); [Campana et al. 2016](#); [Coti Zelati et al. 2018](#)). However, subsequent observations of the prototypical tMSP PSR J1023+0038 (henceforth J1023) revealed a clear anticorrelated variability pattern between the X-ray and radio emissions ([Bogdanov et al. 2018](#)). This indicates that compact jet radiation can hardly account for the whole radio emission and that additional short-lived ejection processes of different origin are likely to operate closer to the NS for $\approx 20\%$ of the time, causing the enhancements in the radio brightness and the switch to the low mode in the X-rays. These enhancements are probably caused by outflows of optically-thin plasma, but the physical mechanism that drives such events is currently not well understood (see [Bogdanov et al. 2018](#) for an extensive discussion; see also [Baglio et al. 2019](#)). It may be related to a rapid displacement (to a greater distance from the NS) of a termination shock that forms due to the interaction between the particle wind ejected by a constantly active rotation-powered MSP and the in-flowing plasma ([Papitto et al. 2019](#)). Alternatively, it may be associated with a switch from a rotation-powered regime to a propeller regime at the transition from the high mode to the low mode ([Veledina et al. 2019](#)).

Recently, we have discovered that the source CXOU J110926.4–650224 (henceforth J1109) shows optical and high-energy emission properties closely resembling those of tMSPs in the X-ray sub-luminous state ([Coti Zelati et al. 2019](#); CZ19 hereafter): broad Balmer and Helium emission

Table 1. Observation log in 2019.

Telescope	Start – End time Mmm DD hh:mm:ss (UTC)	Exposure (ks)
<i>XMM-Newton</i> /EPIC MOS1	Jun. 14 18:46:04 – Jun. 15 02:26:26	26.8
<i>XMM-Newton</i> /EPIC MOS2	Jun. 14 18:46:25 – Jun. 15 02:26:31	26.8
<i>XMM-Newton</i> /EPIC pn	Jun. 14 19:23:42 – Jun. 15 02:30:37	24.9
<i>XMM-Newton</i> /OM ^(a)	Jun. 14 18:54:26 – Jun. 15 02:29:47	25.5
MeerKAT	Jun. 14 15:31:32 – Jun. 14 23:23:45	28.4
<i>XMM-Newton</i> /EPIC MOS1	Jun. 15 14:24:17 – Jun. 16 00:51:19	36.5
<i>XMM-Newton</i> /EPIC MOS2	Jun. 15 14:24:40 – Jun. 16 00:51:25	36.5
<i>XMM-Newton</i> /EPIC pn	Jun. 15 15:01:55 – Jun. 16 00:51:39	34.4
<i>XMM-Newton</i> /OM ^(b)	Jun. 15 16:56:13 – Jun. 16 00:24:40	25.1
MeerKAT	Jun. 15 14:44:26 – Jun. 15 22:31:34	28.1
<i>Swift</i> /XRT	Sep. 6 21:01:34 – Sep. 6 21:29:56	1.7
<i>Swift</i> /XRT	Sep. 6 22:37:03 – Sep. 6 23:04:56	1.7
<i>Swift</i> /XRT	Sep. 7 00:14:23 – Sep. 7 00:17:53	0.2
ATCA	Sep. 6 22:36:30 – Sep. 7 07:09:20	30.8

Notes. ^(a)Seven exposures were acquired, with lengths ranging from 1.2 to 4.3 ks. ^(b)The OM observation started about 8 ks after the EPIC observation, due to an instrument anomaly. Seven exposures were acquired, with lengths from 1.2 to 4.0 ks.

lines in the optical spectrum displaying variable profiles at different epochs, indicating the presence of an accretion disk in the system; a trimodal variability pattern in the X-ray emission around an average luminosity of $L_X \approx 2 \times 10^{34} \text{ erg s}^{-1}$ (assuming a distance of 4 kpc); a spatial association with a gamma-ray source listed in the preliminary *Fermi*/LAT 8-yr point source list with a luminosity akin to those of the transitional MSPs in the accretion disk state. J1109 was undetected at radio wavelengths in shallow observations with the Australia Telescope Compact Array (ATCA) coordinated with a *NuSTAR* X-ray pointing, seemingly at odds with what has been seen in the tMSPs. However, the flux upper limits were consistent with the radio luminosity expected for tMSPs at similar X-ray luminosities ([Gallo et al. 2018](#)).

This manuscript presents the results of new, simultaneous observations of J1109 with the *XMM-Newton* satellite and the MeerKAT telescope, complemented by subsequent simultaneous X-ray and radio observations with the *Neil Gehrels Swift* Observatory and ATCA. We describe the observations and the data analysis in Sect. 2 and report the results in Sect. 3. A discussion and conclusions follow in Sects. 4 and 5.

2. Observations and data processing

Table 1 reports the journal of the observations. In the following, we give details on the two campaigns, and describe the data processing and analysis. We adopt the following position for J1109: RA = 11^h09^m26^s.40, Dec = –65°02′24″.80 (J2000.0¹).

2.1. Observations in June 2019

2.1.1. *XMM-Newton*

The European Photon Imaging Cameras (EPIC; [Strüder et al. 2001](#); [Turner et al. 2001](#)) and the Optical/UV Monitor Tele-

¹ This was derived by applying a linear correction to the position quoted in the early version of the third data release (EDR3) from the *Gaia* space telescope (which is given at the reference epoch J2016.0), based on the source proper motion, $\mu_{\text{RA}} = 1.17 \pm 0.96 \text{ mas yr}^{-1}$, $\mu_{\text{Dec}} = -1.60 \pm 0.67 \text{ mas yr}^{-1}$, and accounting for uncertainties in the absolute *Gaia* positions ([Gaia Collaboration 2021](#)). The 1σ uncertainties on the position so evaluated are $\sigma_{\text{RA}} \approx 14 \text{ mas}$, $\sigma_{\text{Dec}} \approx 11 \text{ mas}$.

scope (OM; Mason et al. 2001) on board *XMM-Newton* observed J1109 twice between 2019 June 14 and 16. The EPIC-MOS cameras were configured in small window mode, the EPIC-pn detector was set in fast timing mode and the OM operated in the fast window mode in white light. The data were processed and analyzed using the Science Analysis Software (SAS v. 19).

We converted the X-ray photons arrival times from the Terrestrial Time (TT) standard to the Coordinated Universal Time (UTC) standard. We discarded data acquired over the first 10 ks of the first observation, owing to strong contamination from background flares, and retained subsequent events within the 0.3–10 keV energy range for the following analysis. For the MOS cameras, we extracted the source photons from a circle of radius 30'' centred on the source position and the background photons from a circle of radius 60'' located on one of the outer CCDs. For the pn, we collected the source photons from a 10-pixel-wide strip oriented along the readout direction of the CCD ($32 < \text{RAW-X} \leq 42$) and the background photons from a 3-pixel-wide region far from the source ($3 < \text{RAW-X} \leq 5$). J1109 was detected at the following net count rates: $0.186 \pm 0.003 \text{ counts s}^{-1}$ (June 14) and $0.159 \pm 0.002 \text{ counts s}^{-1}$ (June 15) with the MOS1; $0.199 \pm 0.003 \text{ counts s}^{-1}$ (June 14) and $0.161 \pm 0.002 \text{ counts s}^{-1}$ (June 15) with the MOS2; $0.580 \pm 0.009 \text{ counts s}^{-1}$ (June 14) and $0.498 \pm 0.005 \text{ counts s}^{-1}$ (June 15) with the pn. We extracted the source light curve by combining the background-subtracted time series acquired over the time intervals covered by the three EPIC cameras simultaneously in the 0.3–10 keV energy range. We extracted the spectra retaining single to quadruple pixel events for the MOS, and single and double pixel events with energy $\geq 0.7 \text{ keV}$ for the pn².

J1109 was detected by the OM only during the last six images in the second pointing at net count rates in the range $\approx 0.4\text{--}0.8 \text{ counts s}^{-1}$. A reliable estimate of the local background level in the OM images where the source was undetected is complicated owing to the presence of a time-variable flux excess at the source position caused by a nearby contaminating extended scattered light feature³. Based on the mean background level over the whole field of view in the single images, we can estimate the following conservative upper limits on the count rates of J1109: $\approx 0.15 \text{ counts s}^{-1}$ for each 4-ks image and $\approx 0.3 \text{ counts s}^{-1}$ for the 1.2-ks image acquired towards the end of the first observing run (at 3σ). We stress, however, that these values are very likely to underestimate the true background level at the source position.

2.1.2. MeerKAT

MeerKAT (Jonas & MeerKAT Team 2016; Camilo et al. 2018; Mauch et al. 2020) observed J1109 twice on 2019 June 14 and 15 using 61 and 60 antennas, respectively. The total exposures were ~ 7.9 and ~ 7.8 h for the first and the second track, respectively (including overheads). The data were recorded at a central frequency of 1.284 GHz with a total bandwidth of 856 MHz split into 4096 frequency channels and an integration time of 8 s. The source PKS 1934–638 (Reynolds 1994) was used for bandpass and flux calibration. The source J0906–6829 (RA = $09^{\text{h}}06^{\text{m}}52^{\text{s}}.23$, Dec = $-68^{\circ}29'39''.90$, J2000) was used for gain calibration during the second epoch.

We flagged the data by applying a dilated hard static mask to remove interference from mobile telecommunications and navigational satellite transmission that contaminate the passband of the MeerKAT *L*-band wideband system, as well as by applying further manual flagging. This resulted in a flagging in excess of 70% for both observations. The flux scale and temporal variability calibrations for the second observation were then bootstrapped to the first observation using a model of the target field derived from self-calibration of the second epoch, so as to minimize relative errors in the flux scales between the two observations.

We then corrected for the residual offset in the average flux scales of a cross-matched selection of compact AGNs detected at a significance $\geq 50\sigma$ on the time-averaged continuum maps of the two epochs ($1\sigma \approx 5 \mu\text{Jy}$ for both epochs). Sources are classified as compact by measuring their peak-to-integrated flux ratio using the Python Blob Detector and Source Finder (PYBDSF; Mohan & Rafferty 2015). A ratio close to unity for a source detected at high significance indicates that the source is unresolved, thus largely not subject to slight changes in the Point Spread Function between epochs. This ensured a relative error in the flux scales below the 1% level between the two epochs. The error on the absolute flux scale was quantified by transfer calibration onto our backup primary calibrator PKS B0407–65, and was found to be at most 7%.

The data were self-calibrated using the DDFACET imager (Tasse et al. 2018) and CUBICAL calibration (Kenyon et al. 2018) software packages. We used the ‘Briggs’ weighting scheme (Briggs 1995) with a robustness parameter of -0.3^4 to create multi-frequency synthesis maps of untapered MeerKAT *uv*-coverages. This resulted in maps with synthesised beams of $7.38'' \times 6.10''$ for the first epoch and $6.70'' \times 5.91''$ for the second epoch. The field is dominated by off-axis direction-dependent calibration artefacts (in the form of radial stripes and rings), which prompted us to perform direction-dependent calibration and peeling after transfer calibration (see Appendix A).

After self-calibration and peeling successfully removed the sidelobe interference contaminating the target position, we subtracted the flux of the remaining AGN population in a field of view of size $2.5^\circ \times 2.5^\circ$ using a 10σ mask, explicitly excluding the target position. This allowed us to create snapshot images via the *clean* imaging task in the Common Astronomy Software Application (CASA; McMullin et al. 2007) to synthesise dirty maps of the residuals centred on the target position, with integration times of 1 min. These maps could be stacked further to obtain exposures of variable duration.

We also made shallowly deconvolved images of the data after self-calibration and peeling to ensure that the light curves extracted from these residual images were not subject to errors stemming from temporal errors in the calibrated flux scales. We picked several compact AGNs detected at high significance close to the target position and extracted average flux light curves to catch instances of substantial calibration errors in the direction-independent electronic gains. We found that the temporal relative errors did not exceed 6% during the two observations.

Figure 1 shows the final image of the field around J1109 extracted from the stack of all the data. We measured a peak flux density of $33 \pm 4 \mu\text{Jy}$ at 1.284 GHz at the position of J1109 in this image, corresponding to a detection significance of $\approx 7.9\sigma$. The estimated peak-to-integrated

² <https://xmmweb.esac.esa.int/docs/documents/CAL-TN-0018.pdf>

³ *XMM-Newton* helpdesk private communication.

⁴ This value was chosen so as to achieve a nearly optimal sensitivity in angular resolution and at the same time to reduce the sidelobes of the MeerKAT point-spread function.

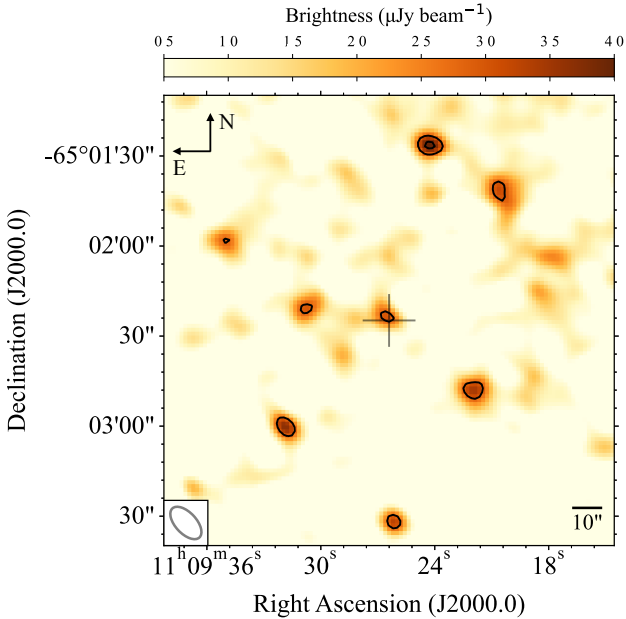


Fig. 1. 1.284-GHz MeerKAT image of the sky region around J1109. The image was obtained from a stack of the data acquired on 2019 June 14 and 15 and its size is $2.5' \times 2.5'$ (north is up and east to the left). The sky region is color-coded according to the values of the brightness at each position, as indicated by the color bar on the top. The rms noise level in this image is $4.2 \mu\text{Jy beam}^{-1}$. Contour levels are drawn at intervals of $(2^{n/2}) \times 30 \mu\text{Jy beam}^{-1}$, where $n=0, 1$. The position of the optical counterpart of J1109 (see Sect. 2.1.1) is marked using a grey cross at the centre of the image. The grey ellipse in the frame in the bottom-left corner represents the shape and size of the synthesised beam, where the major axis is $13.2''$, the minor axis is $7.0''$, and the major axis is located at a position angle of 43.0° measured from north towards east.

flux ratio, ≈ 1.8 , is indicative of compact emission. We fit for the position of this emission using PYBDSF adopting an island cutoff of 3σ and a confidence cutoff of 5σ , and derived the following position: RA = $11^{\text{h}}09^{\text{m}}26^{\text{s}}53 \pm 1^{\text{s}}15$, Dec = $-65^\circ 02' 23''.65 \pm 0''.93$ (J2000.0). This is compatible with the position derived from *Gaia* (and also from *Chandra* X-ray data; see CZ19) within the uncertainties.

2.2. Observations in September 2019

2.2.1. Swift XRT

The *Swift* X-ray Telescope (XRT; Burrows et al. 2005) observed J1109 in the photon counting mode starting on 2019 September 6 at 21:01:34 UTC. The observation was split into three snapshots, resulting in a total elapsed time of ≈ 11.8 ks. The second and the third snapshots were entirely covered by the ATCA observations (see Table 1). The data were processed with standard screening criteria. J1109 was detected at a net count rate of $0.040 \pm 0.003 \text{ counts s}^{-1}$ over the energy range 0.3–10 keV, corresponding to a signal-to-noise ratio of $S/N \approx 10.5$. The net count rates in the single snapshots were 0.043 ± 0.005 , 0.039 ± 0.005 and $0.03 \pm 0.01 \text{ counts s}^{-1}$ (0.3–10 keV), that is, consistent with each other within the uncertainties. Using the whole data set, we extracted the spectrum of J1109 from a circle of radius $47.2''$ centred on the target and the background spectrum from a source-free annulus with radii of $94.4''$ and $188.8''$, also centred on the target.

2.2.2. ATCA

We observed the field of J1109 with the ATCA on 2019 September 6–7, when the telescope was in an extended 6 km ($6C^5$) configuration. The observations were recorded simultaneously at central frequencies of 5.5 and 9 GHz, with 2 GHz of bandwidth at each central frequency. PKS 1934–638 (Reynolds 1994) was used for primary bandpass and flux calibration, while PKS 1059–63 was used for phase calibration. The data were edited for radio frequency interference (RFI) and instrumental issues, calibrated, and imaged following standard procedures in the CASA package. Imaging was carried out with a range of weightings (Briggs robustness parameters of 0, 1, and 2) in an attempt to maximise the image sensitivity and minimise the minor noise effects from a nearby bright source.

J1109 was not detected in these observations, with $3\text{-}\sigma$ upper-limits of $18 \mu\text{Jy}$ at both 5.5 and 9 GHz. To maximise the image sensitivity, we stacked both bands together, which also resulted in a non-detection with a $3\text{-}\sigma$ upper limit of $15 \mu\text{Jy}$ (centred at 7.25 GHz). Stacking the ATCA images acquired in 2019 with those taken in 2018 (see CZ19) resulted in our most sensitive image, but also provided a non-detection, yielding a $3\text{-}\sigma$ upper-limit of $12 \mu\text{Jy}$ at 7.25 GHz.

3. Results

3.1. Multi-band variability

The top panel of Fig. 2 shows the X-ray light curve of J1109. It displays a trimodal variability pattern that is remarkably akin to that observed in previous observations (CZ19), with the switches between the different modes occurring on timescales as short as tens of seconds. Here, we single out the different mode time intervals adopting the following thresholds for the net X-ray count rates (CR) measured in time bins of 50 s: $0.4 \text{ counts s}^{-1} \leq \text{CR} < 2.0 \text{ counts s}^{-1}$ for the high mode; $\text{CR} < 0.4 \text{ counts s}^{-1}$ for the low mode; $\text{CR} \geq 2.4 \text{ counts s}^{-1}$ for the flaring mode. At some point during the second observation, the source was caught in the low mode for a duration of about 50 min – by far the longest period of low mode hitherto observed for this source. Later in the observation, the source underwent three short-lived flaring episodes. The count rate registered at the peak of the second event, $\approx 7 \text{ counts s}^{-1}$, was larger than those measured for the brightest flares in the previous *XMM-Newton* observation in 2018 by a factor of >2 , making this episode the X-ray flare with the highest net count rate at peak so far detected from J1109. The corresponding light curve displayed a rather complex morphology, with at least three structured peaks detected within ≈ 150 s on timescales as short as 10 s (see the inset in Fig. 3).

We fit an absorbed power law (PL) model to the background-subtracted EPIC spectra of J1109 from the two observations jointly using the Xspec software (v. 12.12.0; Arnaud 1996) to estimate the source average X-ray flux. The photoelectric absorption by the interstellar medium was described using the Tuebingen-Boulder model (Wilms et al. 2000), and the absorption column density was held fixed to $N_{\text{H}} = 5.3 \times 10^{21} \text{ cm}^{-2}$ in the fits (see CZ19). A renormalisation factor was included in the fits to account for intercalibration uncertainties across the EPIC cameras, yielding mismatches of $<10\%$. Results are reported in Table 2. The averaged unabsorbed flux, $F_{\text{X}} \approx 3.5 \times 10^{-12} \text{ erg cm}^{-2} \text{ s}^{-1}$ (0.3–10 keV) translates into a luminosity of $L_{\text{X}} \approx 7 \times 10^{33} d_4^2 \text{ erg s}^{-1}$ (0.3–10 keV), where d_4 is the source dis-

⁵ https://www.narrabri.atnf.csiro.au/operations/array_configurations/configurations.html

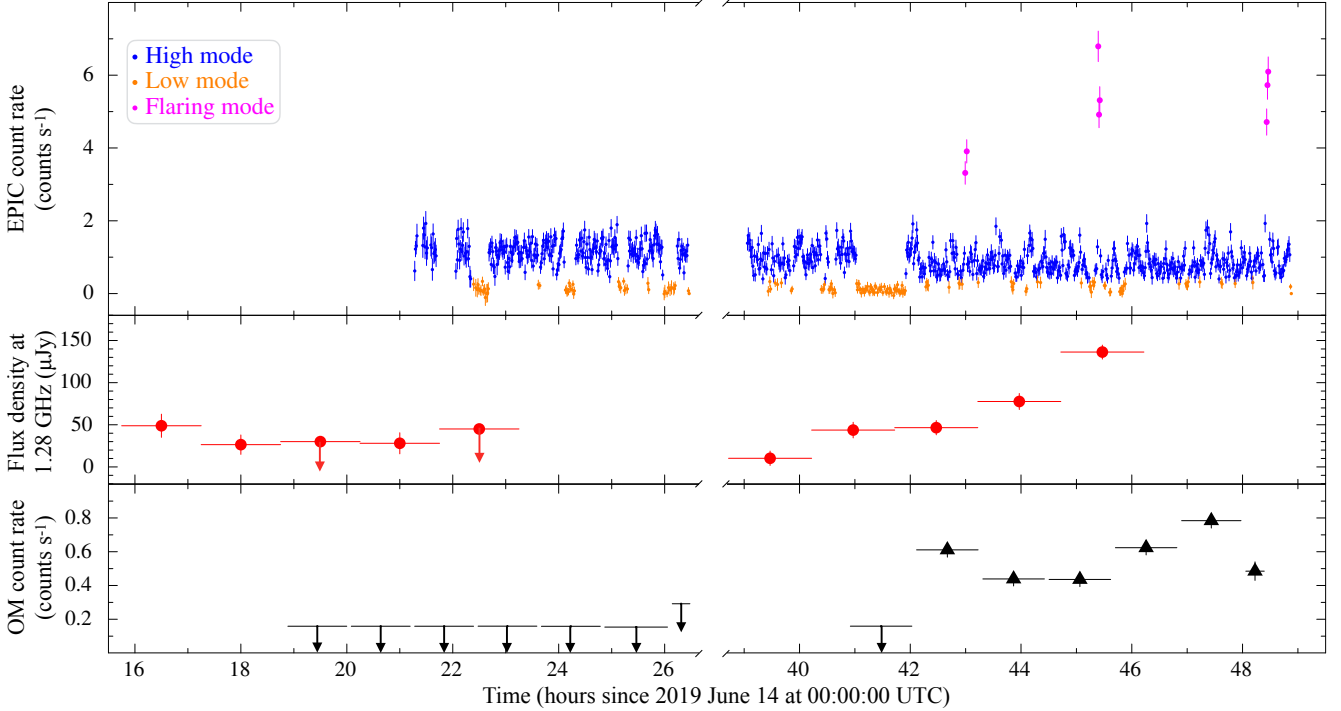


Fig. 2. Multi-band light curves of J1109 on 2019 June 14–16. The X-ray light curve (*top*) is in the 0.3–10 keV energy band and is binned at 50 s. The flaring, high and low modes intervals are depicted in magenta, blue and orange, respectively (see the text for their definition). The radio light curve (*middle*) is in the *L* band (central frequency of 1.284 GHz) and is binned at 1.5 h. The optical light curve (*bottom*) is in white light and was extracted using the net count rates measured in the single images (of lengths of 4 or 1.2 ks). Upper limits are reported for the images where the source was undetected. In all panels, error bars represent 1σ uncertainties, while upper limits are given at a confidence level of 3σ .

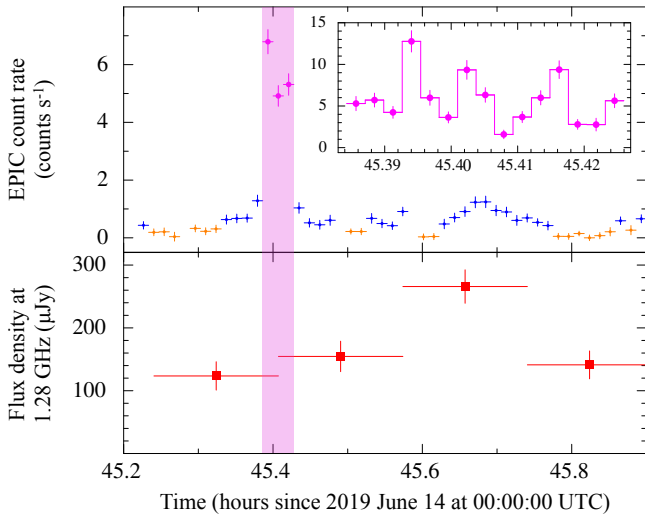


Fig. 3. Zoom of the light curves around the epoch of the brightest X-ray flare (*top*; time bin of 50 s) and the radio flare (*bottom*; time bin of 10 min). The X-ray modes are color-coded as in Fig. 2. The shaded area in magenta marks the epoch of the X-ray flare. The inset in the top panel shows a further zoom of the X-ray light curve at the epoch of the X-ray flare and is binned at 10 s. In all panels, error bars represent 1σ uncertainties.

tance in units of 4 kpc and isotropic emission is assumed (see Sect. 3.3 for a discussion on the source distance). We also evaluated the X-ray flux in each of the modes via a count rate-resolved spectral analysis of the data (see again Table 2).

The faintness of the radio counterpart prevented us to probe the presence of variability in the radio emission detected by MeerKAT on the same timescale of the X-ray mode switching.

Table 2. X-ray spectral properties of J1109 on 2019 June 14–16.

Emission state ^(a)	Γ ^(b)	F_X ^(c) (10^{-12} erg cm $^{-2}$ s $^{-1}$)	χ^2_{red} (d.o.f.)
Average	1.60 ± 0.01	3.53 ± 0.03	1.07 (209)
High mode	1.60 ± 0.01	3.91 ± 0.04	1.12 (234)
Low mode	1.5 ± 0.1	0.60 ± 0.03	0.59 (34)
Flaring mode	1.76 ± 0.05	19.5 ± 0.5	0.95 (50)

Notes. ^(a)The spectra were fitted using an absorbed PL model with the absorption column density held fixed to $N_H = 5.3 \times 10^{21}$ cm $^{-2}$. ^(b)Best-fitting photon index for the absorbed PL model. ^(c)Unabsorbed flux over the 0.3–10 keV energy band.

Nonetheless, we investigated possible changes by computing the flux density in images extracted over time intervals of variable length within the range 10 min–2.5 h. The time intervals of 1.5 h provide the best trade-off between time resolution and S/N in order to characterize variability over the time span covered by our observations. This light curve, shown in the middle panel of Fig. 2, reveals gradual variations in the flux by a factor of ≥ 5 . In particular, the source was undetected during a couple of time intervals on June 14 and was brighter during the second observation on June 15. A closer inspection of the time series on June 15 revealed that the second X-ray flaring activity took place ≤ 15 min before a sharp peak in the radio emission (with a flux density of 266 ± 27 μ Jy over a 10-min interval; Fig. 3).

The optical faintness of J1109 and the presence of a closely extended scattered light feature in the OM images resulted in non-detections for most of the time span covered by the *XMM-Newton* observations. Even in the time intervals where optical emission was detected in the second part of the second observation, the net count rates were too small to enable a detailed study

of variability on timescales comparable with those of the X-ray mode switching. While mild variability in the optical intensity can be seen between these images, no evidence for a significant flux enhancement was found around the epoch of the flares at X-ray and radio wavelengths, possibly due to the long integration time of the OM image (≈ 4 ks; see the bottom panel in Fig. 2). However, recent multi-band, high-time resolution photometric observations of J1109 using ULTRACAM mounted on ESO-NTT revealed that the source indeed also shows optical flaring activity on similar timescales (Coti Zelati et al., in prep.). Hence, a higher time resolution is required to investigate possible connections (including correlations and lags) between the X-ray, radio and optical emissions during flares.

Overall, the radio and optical fluxes appear to be higher towards the end of our observing run on 2019 June 15, when the source spent most of the time in the X-ray high and flaring modes (Fig. 2). To assess the presence of possible correlated or anticorrelated variability between the radio and X-ray emissions, we adopted two different approaches on the data taken on June 15. Firstly, we performed the Spearman and Kendall τ rank correlation tests (Spearman 1904; Kendall 1938) on the values of the radio fluxes and the X-ray count rates measured over strictly simultaneous 30 min-long time intervals. We obtained two-sided p -values of ≈ 0.40 and ≈ 0.31 , respectively, meaning that we cannot reject the null hypothesis that the two variables are uncorrelated at a high confidence level. Secondly, we measured the radio fluxes in the stacked images acquired during the periods of X-ray high mode as well as in the image acquired during the 50-min long period of X-ray low mode. We measured averaged flux densities of $59 \pm 5 \mu\text{Jy}$ (12.0σ) in the former case and $50 \pm 12 \mu\text{Jy}$ (4.2σ) in the latter case, that is, compatible with each other within the uncertainties⁶. Based on the above analyses, we conclude that no clear evidence for a significant correlated or anticorrelated variability is found between the radio and X-ray emissions on the sampled timescales.

3.2. Searches for radio flares in the ATCA data

A radio flare as bright as the one detected in our MeerKAT data (see Fig. 2) should be easily at reach of the ATCA observations. Hence, we separated our ATCA observations into ≈ 30 -min time intervals to search for any such radio flares. For all time intervals but one, no radio source was detected at the position of J1109, with typical $3\text{-}\sigma$ upper-limits of $80 \mu\text{Jy}$. During one time interval on September 7 (between 02:54:00 and 03:36:00 UTC), we see a marginal detection consistent with the position of J1109 at a flux density of $94 \pm 25 \mu\text{Jy}$ (3.8σ) at 7.25 GHz. However, the limited instantaneous uv-coverage of ATCA resulted in a high image noise and an elongated beam, making it difficult to conclusively determine if the detection was real. Refining the time range, changing image weighting, fitting for a point source in the uv-plane, and limiting the image to just one of the observing bands (5.5 or 9 GHz) did not enhance this possible detection. Hence, despite its detection fitting within the behaviour observed with MeerKAT, we cannot convincingly determine whether this detection was real and we do not consider it further in our discussion, pending a higher significance detection at these frequencies in the future.

We note that the ATCA observations were taken at an epoch where J1109 was in the same X-ray sub-luminous state observed

a few months before during our *XMM-Newton* and MeerKAT observing campaign. Indeed, the background-subtracted X-ray spectrum acquired during the simultaneous *Swift*/XRT observations was well described by an absorbed PL model with $\Gamma = 1.5 \pm 0.2$ (1σ c.l.) and the average unabsorbed flux, $F_X \approx 3.3 \times 10^{-12} \text{ erg cm}^{-2} \text{ s}^{-1}$ (0.3–10 keV), was compatible with that measured in all previous X-ray observations during the accretion disk state (Fig. 12 by CZ19).

3.3. The radio brightness of J1109

The simultaneous *XMM-Newton* and MeerKAT observations allow us to place J1109 on the X-ray versus radio luminosity plane for accreting compact objects. The zero-point corrected value for the source parallax has been recently updated to $\varpi = 449 \pm 637 \mu\text{as}$ in the *Gaia* EDR3 (Lindegren et al. 2021; Gaia Collaboration 2021). For such a large uncertainty, the value for the inferred distance depends heavily on the assumed prior. In the hypothesis of an exponentially decreasing space density prior, this value converts to a median distance of 3.4 kpc, with a 1σ confidence interval of 1.9–6.6 kpc. Assuming instead the photo-geometric prior introduced by Bailer-Jones et al. (2021), we obtain a median distance of 11.1 kpc and a 1σ confidence interval of 8.9–13.9 kpc⁷. We thus computed the X-ray and radio luminosities (both averaged and separately for the high and low X-ray modes) assuming conservatively two different values for the source distance, 4 and 11 kpc. Lacking any information on the radio spectral shape, we also assumed a flat spectrum as observed in other tMSPs in the accretion disk state (see e.g. Deller et al. 2015) and in most accreting X-ray binaries in the hard state to rescale the radio luminosity at 5 GHz (i.e. we assumed a spectral index of $\alpha = 0$, where the flux density F_ν scales with the observing frequency ν as $F_\nu \propto \nu^\alpha$). The region occupied by J1109 on the L_X – L_R plane (Fig. 4) is consistent with that of other tMSPs and black hole (BH) binaries in the hard state, providing further evidence that the tMSPs are generally brighter in the radio band than other accreting NSs for a given X-ray luminosity.

4. Discussion

We have presented the discovery of a variable radio counterpart to the tMSP candidate CXOU J110926.4–650224. Such a detection was achieved in the L -band using the MeerKAT interferometer, while the source was in a X-ray sub-luminous state according to simultaneous observations with *XMM-Newton*. The radio counterpart displayed variability on timescales of hours as well as a 10-min flare occurring just a few minutes after the detection of at least three consecutive intense flashes of X-rays within a time span of ~ 2.5 min. No evidence for emission at similar intensity levels was found at higher radio frequencies in multi-epoch observations performed with the ATCA (see also CZ19). This is indicative either of a steep averaged radio spectrum ($\alpha \lesssim -0.5$) or, more likely, of variability across different epochs (assuming a flat averaged spectrum, $\alpha \approx 0$, at all epochs). In fact, changes by a factor of ≈ 2 and $\gtrsim 3$ in the average flux density have been observed at distinct epochs in the tMSP

⁷ This prior accounts at once for the parallax, colour and apparent magnitude quoted in EDR3 by exploiting the fact that stars of a given colour have a restricted range of probable absolute magnitudes plus extinction. In the case of J1109, the bulk of the optical emission is provided by the accretion disk rather than by the companion star, making the source bluer and brighter (see CZ19 for more details on optical spectroscopy of this system). Therefore, the distance derived for J1109 using this prior is likely to be subject to large uncertainties.

⁶ We note that these values are higher than the averaged flux density of $\approx 33 \mu\text{Jy}$ measured using the whole data sets. This discrepancy is due to the long-timescale variability in the radio emission, which yields a flux that is substantially higher on June 15 than on June 14 on average.

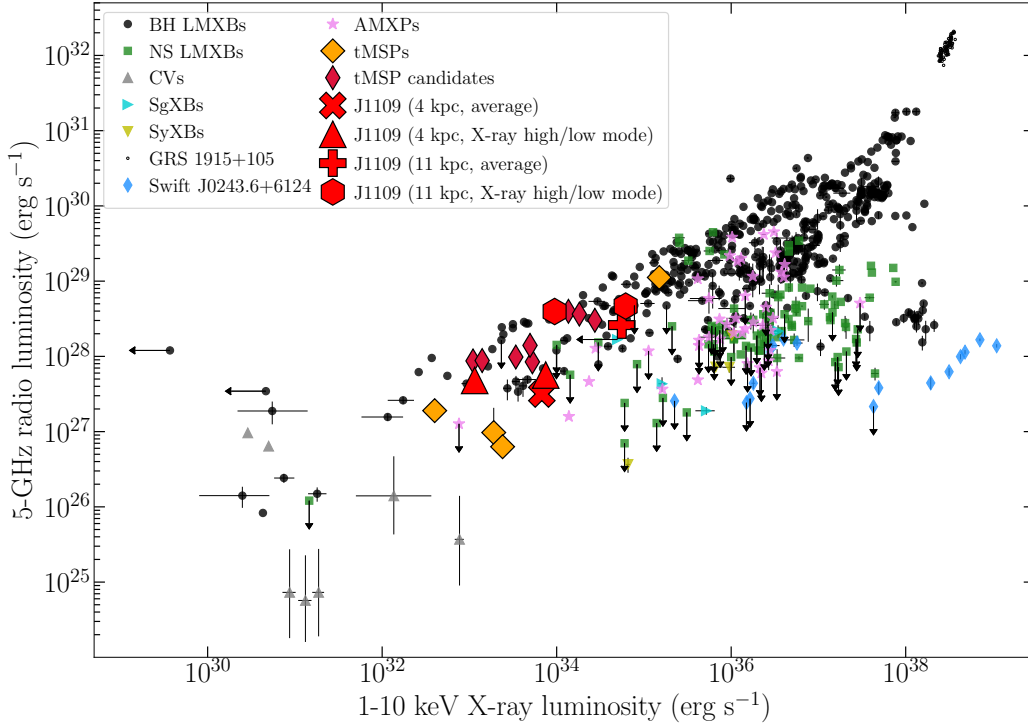


Fig. 4. Radio and X-ray luminosities for different classes of binary systems harbouring different types of accreting compact objects, including low-mass X-ray binaries with BHs and NSs accretors (BH LMXBs, NS LMXBs), cataclysmic variables (CVs), supergiant X-ray binaries (SgXBs), symbiotic X-ray binaries (SyXBs), the peculiar Be X-ray binary Swift J0243+6124, accreting millisecond X-ray pulsars (AMXPs) and known and candidate tMSPs in the disk state. Values are derived from simultaneous or quasi-simultaneous (within 1–2 d) radio and X-ray observations, and are taken from Bahramian et al. (2018) with updates from Bassi et al. (2019), Coti Zelati et al. (2019), Gusinskaia (2019), Parikh et al. (2019), Bright et al. (2020), Gusinskaia et al. (2020a,b), Hewitt et al. (2020), Li et al. (2020), Tremou et al. (2020), Williams et al. (2020), Xie et al. (2020), van den Eijnden et al. (2020, 2021), de Haas et al. (2021), Carotenuto et al. (2021), Motta et al. (2021), Paduano et al. (2021). Values for J1109 are plotted separately for the averaged emission and for the emission during the high and low X-ray modes. Error bars on data points (when available) indicate 1σ uncertainties, and are smaller than the marker size for most of the data points (including those corresponding to J1109). Upper limits are marked using arrows.

J1023 (Deller et al. 2015) and in the candidate 1RXS J154439.4–112820 (J1544; Jaodand 2019), respectively.

No obvious correlated or anticorrelated variability pattern was detected between the radio and X-ray emissions in our MeerKAT and *XMM-Newton* data. However, the radio variability properties, their connection with the emission observed at other wavelengths and the timescales involved may differ from source to source. Substantial, rapid changes in the radio emission from a tMSP were first reported by Ferrigno et al. (2014), who detected variations in the radio flux of the ‘swinging pulsar’ IGR J18245–2452 (J1824) by a factor of ~ 3 over one hour or so during its X-ray outburst in 2013. Moreover, these observations were quasi-simultaneous to X-ray observations and hinted at a possible anti-correlation between the radio and X-ray emissions. More recently, simultaneous X-ray and radio observations of the tMSP J1023 in the X-ray sub-luminous state revealed a highly reproducible, anticorrelated variability pattern between the emissions in the two bands: the switches from the high to the low X-ray modes were always accompanied by enhancements in the radio brightness, with a duration that matches the low mode interval. These rebrightenings were detected using the Very Large Array at frequencies in the range 8–12 GHz (i.e. higher than those probed for J1109 by MeerKAT) and were associated with an evolution of the radio spectrum from inverted to relatively steep over the course of several minutes. Sporadic minutes-long radio flares were also observed (Bogdanov et al. 2018). A similar anti-correlation was also found in the candi-

date J1544 (Gusinskaia 2019), but not in the other candidate 4FGL J0427.8–6704 (J0427; Li et al. 2020). We note, however, that J0427 showed a rather different phenomenology compared to the other tMSPs. Indeed, it was observed to spend most of the time in a flaring mode in the X-ray, UV and optical bands without showing the characteristic X-ray mode switching and displayed only modest variability in the radio emission on timescales as short as hours, possibly correlated with the X-ray flaring activity (Li et al. 2020). Very recently, the *Fermi* source 4FGL J0540.0–7552 (J0540) and the X-ray source NGC 6652B in the globular cluster NGC 6652 have been identified as tMSP candidates characterised by a multiband flaring activity that is remarkably similar to that observed in J0427 (Strader et al. 2021; Paduano et al. 2021). J0540 has not been observed at radio frequencies yet. Future coordinated multiband observations of this system including radio interferometers may allow the detection of radio emission and an assessment of a possible connection with the flaring emission detected at higher energies. NGC 6652B has been observed in the radio band at different epochs and displayed variations in the radio brightness by a factor of ~ 2 on timescales of months. Additionally, simultaneous X-ray and radio observations detected numerous X-ray flares and a number of radio flares with typical durations of a few hundreds of seconds. However, no evidence for a significant correlation between these emissions was found.

The drop in the X-ray flux when switching from the high mode to the low mode is comparable in J1109 and the

prototypical tMSP J1023 (a factor of ≈ 7 ; see Table 2 and Papitto et al. 2019 and references therein). However, the variability properties of the radio emission are seemingly different in the two systems. On the one hand, no obvious rebrightening in the radio band was observed in J1109 during the periods of X-ray low mode. On the other hand, enhancements in the radio brightness by a factor of ~ 3 on average were detected in the case of J1023 during all the periods of X-ray low mode, which lasted typically only a few minutes (i.e. they were much shorter than the 50 min-long episode of X-ray low mode observed from J1109 during our campaign; see Bogdanov et al. 2018). We note that our non-detection of any significant radio rebrightening during the periods of X-ray low mode in J1109 is not due to limitations in the instrumental detection sensitivity: the rms noise level attained by MeerKAT during the long episode of X-ray low mode in the second observation was $\approx 12 \mu\text{Jy}$, hence a concurrent increase in the radio flux density of a similar extent as seen in J1023 could have been detected at a confidence level of $\geq 10\sigma$. Overall, our analysis seems thus to suggest that the mechanism responsible for the radio emission at low frequencies in J1109 may not be directly connected with the process driving the X-ray mode switching.

Assuming that the X-ray mode switching in the tMSPs truly operates close to the NS as suggested by recent studies (Papitto et al. 2019; Veledina et al. 2019; Campana et al. 2019), we may speculate that the bulk of the low-frequency emission of J1109 is provided by compact jet radiation and that possible additional ejection processes close to the NS (similar to those invoked for J1023) may still be at work but without producing a detectable increase in the radio brightness above the jet emission level. This scenario may well be possible if the ejected material remains optically thick to synchrotron self-absorption at the low frequencies probed by MeerKAT (~ 1.3 GHz) over the whole duration of the X-ray low modes. In the future, deeper multi-frequency radio observations of J1109 with the Square Kilometre Array (SKA) coordinated with X-ray observations may allow testing for this scenario by characterising the broadband spectral evolution of the radio emission during the X-ray low modes. Additionally, a detection of possible turnovers in the spectral slope that lead to flux rebrightenings only above certain radio frequencies can also provide a valuable test for this scenario.

The nature of the enhanced radio emission observed in J1109 towards the end of 2019 June 15 is perhaps more uncertain. It may be associated with optically thin synchrotron radiation from discrete blobs of plasma ejected away from the compact object due to the formation of a transient accretion-driven jet or, alternatively, due to a mechanism ultimately connected with the presence of an active rotation-powered pulsar. The peculiar properties of the pulsed emission of J1023 at optical and X-ray wavelengths, in fact, were recently interpreted in terms of synchrotron radiation from particles accelerated at a termination shock that forms due to the interaction between the particle wind ejected from the pulsar and plasma inflowing in the inner disk regions (a few hundreds of kilometers away from the pulsar, just outside the light cylinder; Papitto et al. 2019; Veledina et al. 2019). In this framework, X-ray emission during flares may be due to temporary enshrouding of the wind by the shock front (see also Campana et al. 2019), possibly due to a sudden increase in the thickness of the inner edge of the accretion disk (Veledina et al. 2019). In this phase, episodes of reconnection of magnetic field lines at the turbulent termination shock may launch outflows of plasmoids. For particularly strong, short-lived X-ray flares, a delayed flaring emission may be expected at radio frequencies

(as observed in J1109 as well as in J1023; see Fig. 3 and Bogdanov et al. 2018) as the plasma quickly expands outwards and becomes progressively more rarefied and transparent to synchrotron radiation even at low frequencies. Magnetic reconnection could also explain the increase in the optical flux observed around the same epoch of the X-ray flares and of the enhanced radio brightness (see Fig. 2).

We can tentatively estimate the physical parameters of the radio synchrotron-emitting plasma during flaring in the hypothesis that no energy is carried away by baryons and the plasma fulfills the equipartition condition, that is, the energy content in electrons balances that in the magnetic field. Assuming for simplicity a symmetric profile for the light curve of the flare (i.e. assuming a flare rise time of ~ 5 min, which is about half the duration of the time bin corresponding to the peak in the radio flux density; see Fig. 3), we can derive a minimum internal energy of $E_{\min} \approx 10^{37} d_4^{8/7}$ erg and a magnetic field of $B \approx 0.3 d_4^{4/7}$ G at equipartition (see Fender 2006). We can also set a conservative lower limit on the linear size of the emitting region of $R > 4 \times 10^{11} d_4$ cm by imposing that the brightness temperature T_b does not exceed the limit of 10^{12} K, above which energy loss by synchrotron self-Compton radiation would become catastrophic (Longair 2011). We obtain instead values of $E_{\min} \approx 10^{36} d_4^{40/17}$ erg, $B \approx 0.3 d_4^{-4/17}$ G and $R \approx 2.6 \times 10^{12} d_4^{16/17}$ cm under the additional hypothesis that the flare peak corresponds to an optical depth transition from thick to thin (see Fender & Bright 2019). While the orbital parameters of J1109 are still unknown, it seems plausible that the two length scales estimated above could be larger than the orbital separation expected for this system⁸, suggesting that the radio flaring emission is likely to be radiated from an extended cloud of plasma. We note, however, that the assumption of equipartition may well be an oversimplification. As a matter of fact, all pulsar wind nebulae detected at high energies are strongly particle-dominated and their magnetization is usually at the level of just a few percent (e.g. Tanaka & Takahara 2010; Torres et al. 2014). Besides, caution should be exerted in overinterpreting the latter estimates in the absence of any measurement of the spectral shape and evolution of the flaring emission.

5. Conclusions

We have presented the discovery of a variable radio counterpart to the tMSP candidate J1109 in multi-epoch coordinated X-ray and radio observations performed when the source was in a X-ray sub-luminous state. J1109 joins the small sample of known and candidate tMSPs for which relatively bright radio emission has been detected in the X-ray sub-luminous state.

Future observations with the SKA may enable a more detailed investigation of variability in the emission of J1109 across a range of radio frequencies and on timescales compatible with those of the X-ray mode switching (see e.g. Braun et al. 2019). A conclusive assessment on the presence or absence of (anti)correlated variability between the radio and X-ray emissions in this system and other candidates will be critical in providing a consistent picture for the mechanisms of mass ejection and accretion in the tMSPs.

Acknowledgements. We thank N. Schartel for approving Target of Opportunity observations with *XMM-Newton* in the Director's Discretionary Time and the *XMM-Newton* Science Operation Center for scheduling and carrying out the

⁸ The orbital separation is of the order of a few 10^{11} cm in the case of J1824, the tMSP with the longest orbital period (Papitto et al. 2013).

observations. We thank S. Goedhart and the staff at the South African Radio Astronomy Observatory (SARAO) for scheduling and carrying out the MeerKAT observations. We thank the reviewer for providing helpful comments. FCZ is supported by a Juan de la Cierva fellowship (IJC2019-042002-I). FCZ, DFT and NR are supported by the Spanish Grant PGC2018-095512-B-I00 and the Catalan Grant SGR2017-1383. FCZ and NR are also supported by the ERC Consolidator Grant ‘MAGNESIA’ (nr. 817661). DdM and AP acknowledge financial support from the Italian Space Agency (ASI) and National Institute for Astrophysics (INAF) under agreements ASI-INAF I/037/12/0 and ASI-INAF n.2017-14-H.0 (PI: Belloni), from INAF ‘Sostegno alla ricerca scientifica main streams dell’INAF’ (PI: Belloni) Presidential Decree 43/2018, and from INAF ‘Towards the SKA and CTA era: discovery, localisation, and physics of transient sources’ (PI: Giroletti) Presidential Decree 70/2016. DAHB is supported by the National Research Foundation (NRF) of South Africa. TDR acknowledges financial contribution from the agreement ASI-INAF n.2017-14-H.0. JL acknowledges the support from the National Natural Science Foundation of China via NSFC-11733009. We acknowledge the International Space Science Institute (ISSI – Beijing), which funded and hosted the international teams ‘The disk-magnetosphere interaction around transitional millisecond pulsars’ and ‘Understanding and unifying the gamma-rays emitting scenarios in high mass and low mass X-ray binaries’. We thank partial support from the COST Action ‘PHAROS’ (CA 16124). The *XMM-Newton* data are available at the European Space Agency (ESA) archive (<http://nxsas.esac.esa.int/nxsas-web>; obs. IDs: 0851180201, 0851180301). The *Swift* data are available at the *Swift* archive (https://www.swift.ac.uk/swift_portal; obs. ID: 00011274002). The MeerKAT observations were obtained under the Open Time proposal SCI-20190418-DB-01 (PI: DAHB). The uncalibrated visibility data are available at the SARAO archive (<https://archive.sarao.ac.za>). The Australia Telescope Compact Array (ATCA) observations were obtained under project code C3007 (PI: FCZ). The uncalibrated visibility data are available at the Australia Telescope National Facility (ATNF) archive (<https://atoa.atnf.csiro.au>). The calibrated MeerKAT data and images that support the findings of this study, the data for the light curves and the values for the data points shown in Fig. 4 of this paper are available from the corresponding author upon reasonable request. *XMM-Newton* is an ESA science mission with instruments and contributions directly funded by ESA Member States and NASA. The *Neil Gehrels Swift* Observatory is a NASA/UK/ASI mission. The MeerKAT telescope is operated by SARAO, which is a facility of the NRF, an agency of the Department of Science and Innovation. The ATCA is part of the ATNF, which is funded by the Australian Government for operation as a National Facility managed by the Commonwealth Scientific and Industrial Research Organisation. We acknowledge the Gomeri people as the traditional owners of the ATCA observatory site. This research has made use of the following software: APLPY v.2.0.3 (Robitaille & Bressert 2012), Astropy v.4.3.1 (Astropy Collaboration 2013, 2018), CASA v.5.6.0 (McMullin et al. 2007), cleanmask v.1.3.1 (<https://github.com/SpheMakh/cleanmask>), Cubical v.1.5.11 (Kenyon et al. 2018), DDFacet v.0.6.0 (Tasse et al. 2018), HEASOFT v.6.29c, katdal v.0.18 (<https://github.com/ska-sa/katdal>), MATPLOTLIB v.3.4.3 (Hunter 2007), NUMPY v.1.21.2 (Harris et al. 2020), pyBDSF v.1.9.1 (Mohan & Rafferty 2015), SAOImageDS9 v.8.2.1 (Joye & Mandel 2003), SAS v.19 (Gabriel et al. 2004), SCIPY v.1.7.1 (Virtanen et al. 2020), Tigger v.1.6.0 (<https://github.com/ska-sa/tigger>), XRONOS v.5.21 (Stella & Angelini 1992), XSPEC v.12.12.0 (Arnaud 1996).

References

- Ambrosino, F., Papitto, A., Stella, L., et al. 2017, *Nat. Astron.*, **1**, 854
- Archibald, A. M., Stairs, I. H., Ransom, S. M., et al. 2009, *Science*, **324**, 1411
- Arnaud, K. A. 1996, *ASP Conf. Ser.*, **101**, 17
- Astropy Collaboration (Robitaille, T. P., et al.) 2013, *A&A*, **558**, A33
- Astropy Collaboration (Price-Whelan, A. M., et al.) 2018, *AJ*, **156**, 123
- Baglio, M. C., Vincentelli, F., Campana, S., et al. 2019, *A&A*, **631**, A104
- Bahramian, A., Miller-Jones, J., Strader, J., et al. 2018, <https://doi.org/10.5281/zenodo.1252036>
- Bailer-Jones, C. A. L., Rybizki, J., Founesneau, M., Demleitner, M., & Andrae, R. 2021, *AJ*, **161**, 147
- Bassa, C. G., Patruno, A., Hessels, J. W. T., et al. 2014, *MNRAS*, **441**, 1825
- Bassi, T., Del Santo, M., D’Ai, A., et al. 2019, *MNRAS*, **482**, 1587
- Blandford, R. D., & Königl, A. 1979, *ApJ*, **232**, 34
- Blandford, R. D., & Payne, D. G. 1982, *MNRAS*, **199**, 883
- Bogdanov, S., Deller, A. T., Miller-Jones, J. C. A., et al. 2018, *ApJ*, **856**, 856
- Braun, R., Bonaldi, A., Bourke, T., Keane, E., & Wagg, J. 2019, ArXiv e-prints [arXiv:1912.12699]
- Briggs, D. S. 1995, *Am. Astron. Soc. Meet. Abstr.*, **187**, 112.02
- Bright, J. S., Fender, R. P., Motta, S. E., et al. 2020, *Nat. Astron.*, **4**, 697
- Burrows, D. N., Hill, J. E., Nousek, J. A., et al. 2005, *Space Sci. Rev.*, **120**, 165
- Camilo, F., Scholz, P., Serylak, M., et al. 2018, *ApJ*, **856**, 180
- Campana, S., & Di Salvo, T. 2018, *Astrophys. Space Sci. Lib.*, **457**, 149
- Campana, S., Coti Zelati, F., Papitto, A., et al. 2016, *A&A*, **594**, A31
- Campana, S., Miraval Zanon, A., Coti Zelati, F., et al. 2019, *A&A*, **629**, L8
- Carotenuto, F., Corbel, S., Tremou, E., et al. 2021, *MNRAS*, **505**, L58
- Coti Zelati, F., Campana, S., Braito, V., et al. 2018, *A&A*, **611**, A14
- Coti Zelati, F., Papitto, A., de Martino, D., et al. 2019, *A&A*, **622**, A211
- de Haas, S. E. M., Russell, T. D., Degenaar, N., et al. 2021, *MNRAS*, **502**, 521
- de Martino, D., Papitto, A., Burgay, M., et al. 2020, *MNRAS*, **492**, 5607
- Deller, A. T., Moldon, J., Miller-Jones, J. C. A., et al. 2015, *ApJ*, **809**, 13
- Fender, R. 2006, *Jets from X-ray Binaries*, **39**, 381
- Fender, R., & Bright, J. 2019, *MNRAS*, **489**, 4836
- Ferrigno, C., Bozzo, E., Papitto, A., et al. 2014, *A&A*, **567**, A77
- Gabriel, C., Denby, M., Fyfe, D. J., et al. 2004, *ASP Conf. Ser.*, **314**, 759
- Gaia Collaboration (Brown, A. G. A., et al.) 2021, *A&A*, **649**, A1
- Gallo, E., Degenaar, N., & van den Eijnden, J. 2018, *MNRAS*, **478**, L132
- Gusinskaia, N. 2019, PhD Thesis, University of Amsterdam, The Netherlands
- Gusinskaia, N. V., Hessels, J. W. T., Degenaar, N., et al. 2020a, *MNRAS*, **492**, 2858
- Gusinskaia, N. V., Russell, T. D., Hessels, J. W. T., et al. 2020b, *MNRAS*, **492**, 1091
- Harding, A. K. 2021, ArXiv e-prints [arXiv:2101.05751]
- Harris, C. R., Millman, K. J., van der Walt, S. J., et al. 2020, *Nature*, **585**, 585
- Hewitt, D. M., Pretorius, M. L., Woudt, P. A., et al. 2020, *MNRAS*, **496**, 2542
- Hill, A. B., Szostek, A., Corbel, S., et al. 2011, *MNRAS*, **415**, 235
- Hunter, J. D. 2007, *Comput. Sci. Eng.*, **9**, 9
- Jaodand, A. D. 2019, PhD Thesis, University of Amsterdam, The Netherlands
- Jaodand, A. D., Hernández Santisteban, J. V., Archibald, A. M., et al. 2021, ArXiv e-prints [arXiv:2102.13145]
- Jonas, J., & MeerKAT Team 2016, *Proceedings of MeerKAT Science: On the Pathway to the SKA*, **25–27 May**, 1
- Joye, W. A., & Mandel, E. 2003, *ASP Conf. Ser.*, **295**, 489
- Kendall, M. G. 1938, *Biometrika*, **30**, 30
- Kenyon, J. S., Smirnov, O. M., Grobler, T. L., & Perkins, S. J. 2018, *MNRAS*, **478**, 2399
- Li, K.-L., Strader, J., Miller-Jones, J. C. A., Heinke, C. O., & Chomiuk, L. 2020, *ApJ*, **895**, 89
- Lindgren, L., Klioner, S. A., Hernández, J., et al. 2021, *A&A*, **649**, A2
- Longair, M. S. 2011, *High Energy Astrophysics*, 3rd edn. (Cambridge: Cambridge University Press)
- Mason, K. O., Breeveld, A., Much, R., et al. 2001, *A&A*, **365**, L36
- Mauch, T., Cotton, W. D., Condon, J. J., et al. 2020, *ApJ*, **888**, 61
- McMullin, J. P., Waters, B., Schiebel, D., Young, W., & Golap, K. 2007, *ASP Conf. Ser.*, **376**, 127
- Mohan, N., & Rafferty, D. 2015, Astrophysics Source Code Library [record ascl:1502.007]
- Motta, S. E., Tremou, E., Fender, R., et al. 2021, *ATel*, **14659**, 1
- Paduano, A., Bahramian, A., Miller-Jones, J. C. A., et al. 2021, *MNRAS*, **506**, 4107
- Papitto, A., & de Martino, D. 2020, ArXiv e-prints [arXiv:2010.09060]
- Papitto, A., & Torres, D. F. 2015, *ApJ*, **807**, 33
- Papitto, A., Ferrigno, C., Bozzo, E., et al. 2013, *Nature*, **501**, 517
- Papitto, A., Ambrosino, F., Stella, L., et al. 2019, *ApJ*, **882**, 104
- Parikh, A. S., Russell, T. D., Wijnands, R., et al. 2019, *ApJ*, **878**, L28
- Reynolds, J. E. 1994, *A Revised Flux Scale for the AT Compact Array*, ATNF Memo, AT/39.3/040
- Robitaille, T., & Bressert, E. 2012, Astrophysics Source Code Library [record ascl:1208.017]
- Smirnov, O. M. 2011, *A&A*, **527**, A106
- Spearman, C. 1904, *Am. J. Psychol.*, **15**, 15
- Stappers, B. W., Archibald, A. M., Hessels, J. W. T., et al. 2014, *ApJ*, **790**, 39
- Stella, L., & Angelini, L. 1992, in *XRONOS: A Timing Analysis Software Package*, eds. V. Di Gesù, L. Scarsi, & R. Bucccheri, et al. (Boston: Springer), 59
- Strader, J., Swihart, S. J., Urquhart, R., et al. 2021, *ApJ*, **917**, 69
- Strüder, L., Briel, U., Dennerl, K., et al. 2001, *A&A*, **365**, L18
- Tanaka, S. J., & Takahara, F. 2010, *ApJ*, **715**, 1248
- Tasse, C., Hugo, B., Mirmont, M., et al. 2018, *A&A*, **611**, A87
- Torres, D. F., Cillis, A., Martín, J., & de Oña Wilhelmi, E. 2014, *J. High Energy Astrophys.*, **1**, 31
- Tremou, E., Corbel, S., Fender, R. P., et al. 2020, *MNRAS*, **493**, L132
- Turner, M. J. L., Abbey, A., Arnaud, M., et al. 2001, *A&A*, **365**, L27
- van den Eijnden, J., Degenaar, N., Russell, T. D., et al. 2020, *MNRAS*, **496**, 4127
- van den Eijnden, J., Degenaar, N., Russell, T. D., et al. 2021, *MNRAS*, **507**, 3899
- Veledina, A., Näätäli, J., & Beloborodov, A. M. 2019, *ApJ*, **884**, 144
- Virtanen, P., Gommers, R., Oliphant, T. E., et al. 2020, *Nat. Meth.*, **17**, 261
- Williams, D. R. A., Motta, S. E., Fender, R., et al. 2020, *MNRAS*, **491**, L29
- Wilms, J., Allen, A., & McCray, R. 2000, *ApJ*, **542**, 914
- Xie, F.-G., Yan, Z., & Wu, Z. 2020, *ApJ*, **891**, 31

Appendix A: Direction-dependent calibration and peeling of the MeerKAT data

Direction-dependent calibration and peeling of the MeerKAT data was accomplished by solving the following radio interferometer measurement equation (RIME):

$$V_{pq}(t) = G_p(t) \left\{ \mathcal{F}[M_{\text{DIE}}] + \sum_{l,m}^{\text{dir}} \Delta_p(v, t, l, m) \mathcal{F}[M(l, m)] \Delta_q^H(v, t, l, m) \right\} G_q^H(t). \quad (\text{A.1})$$

The term on the left-hand side V_{pq} represents the visibility observed by a baseline formed by a pair of antennas p and q ,

where $p, q \in [1, \dots, N_A]$ and N_A is the total number of antennas in the interferometer. Eq. (A.1) simultaneously solves for the temporal electronic gains G_p and G_q towards all the flux in the field unaffected by direction-dependent errors ($\mathcal{F}[M_{\text{DIE}}]$), as well as for the direction-dependent differential gains Δ_p and Δ_q for a number of sky regions in the field (e.g. polygons) tagged by the user (l, m are the ‘direction cosines’ toward the sky; the superscript ‘ H ’ denotes the Hermitian transpose; see e.g. [Smirnov 2011](#) for more details on the RIME formalism). The flux contained within each of these regions ($\mathcal{F}[M(l, m)]$) is predicted through targeted faceting from the sky model produced by DDFACET ([Tasse et al. 2018](#)). This approach of simultaneous calibration and peeling taking into account all available flux limits the suppression of unmodelled sky flux that is typically seen in traditional phase-steering and peeling methods using just a model of the source affected by direction-dependent calibration errors.